CrossMark

ORIGINAL PAPER

Synthesis and Characterization of Fe-Doped CeO_2 for Application in the NO Selective Catalytic Reduction by CO

**Rodrigo Brackmann[1] · Fabio Souza Toniolo[1] · Martin Schmal[1]**

Abstract We prepared $Ce_{1-x}Fe_xO_{2-\delta}$ mixed oxides (x = 0; 0.05; 0.1; 0.15 and 0.2) by Pechini method and we characterized the materials by X-ray fluorescence, X-ray diffraction, N_2 physisorption, UV–Vis diffuse reflectance spectroscopy and scanning electron microscopy. The mixed oxides were evaluated in the selective catalytic reduction of NO by CO. The characterization showed that the synthesis method is suitable for obtaining oxides with desired stoichiometry and single phase solid solution for all Fe contents. The catalytic tests allowed to conclude that $Ce_{1-x}Fe_xO_{2-\delta}$ are promising for NO abatement by CO due to the improvement of the physicochemical properties of the synthesized solid solutions by Fe incorporation, such as decreasing crystallite sizes and increasing oxygen vacancies. $Ce_{1-x}Fe_xO_{2-\delta}$ mixed oxides were able to dissociate NO even at room temperature due to the presence of the anionic vacancies. The increase of iron content in the mixed oxides enhanced the catalytic activity and selectivity to N_2.

Keywords Ceria · Mixed oxides · Oxygen vacancies · NO reduction · Environmental catalysis

1 Introduction

NO_x is a term that includes the most dangerous nitrogen oxides to the environment and to the human health (nitric oxide—NO, nitrous oxide—N_2O and nitrogen dioxide—NO_2) [1, 2]. N_2O is a powerful greenhouse gas which has potential for global warming 300 times greater than CO_2 [3]. NO initiates the stratospheric ozone destruction cycles [2] and NO_2 is very toxic, which can cause pulmonary edema, alveolar hemorrhage, respiratory failure and even death [4].

Burning of fossil fuels such as coal and oil-derived products (gasoline and diesel) emits large amounts of NO_x, CO, CO_2 and unburned hydrocarbons into the atmosphere. Therefore, research in NO_x abatement became more significant in recent decades and the selective catalytic reduction of NO by CO (NO-SCR by CO) (Eq. 1) is one of the most studied reactions for the abatement of NO_x emissions.

$$NO + CO \rightarrow 1/2N_2 + CO_2 \qquad (1)$$
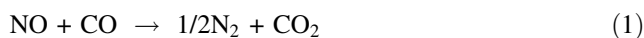
The general trend of NO_x abatement contemplates the development of new materials to meet stringent environmental regulations [1]. Ceria-based materials (CeO_2) are promising and enable redox reactions, such as NO-SCR by CO, due to the ability to absorb and release quick and continuously oxygen from crystal lattice, changing its composition between CeO_2 and CeO_{2-x} via oxidation and reduction cycles [5].

However, as reported in literature [6] sintering of pure CeO_2 occurs at high temperatures causing loss of its oxygen storage capacity (OSC). In this sense, the enhancement of the thermal durability and improvement of the OSC of CeO_2 based materials has been extensively investigated [7]. The incorporation of transition metals or rare earths

✉ Martin Schmal
schmal@peq.coppe.ufrj.br

[1] Chemical Engineering Program, Laboratory Nucleus of Catalysis COPPE/UFRJ, Federal University of Rio de Janeiro, Ilha do Fundão, C.P. 68502, Rio de Janeiro CEP 21941-914, Brazil

into the CeO_2 has been suggested as alternative to stabilize the structure. Another important effect of cationic doping is the increase in the number of structural defects (e.g., oxygen vacancies which are extrinsic defects), which leads to materials with higher OSC [6].

The modified CeO_2 with Fe^{+3} is in particular an interesting catalytic system due to the Ce–Fe synergy that occurs by combining the redox behavior of cerium (Ce^{+4}/Ce^{+3}) and iron (Fe^{+3}/Fe^{+2}) [8]. Several authors have explored these redox properties of Ce–Fe mixed oxides in many reactions such as CO and CH_4 oxidation [8–10], direct NO decomposition [11], mercury oxidation [12], soot combustion [13, 14], Fischer–Tropsch synthesis [15, 16] and N_2O decomposition [17].

Liu et al. [18] suggested that the NO molecule can be dissociated by oxygen vacancies, a necessary step for its abatement. However, the mechanisms on Ce-based mixed oxides are still under debate. Hong et al. [11] showed that the activity of Ba-loaded Ce–Fe mixed oxides for NO decomposition is related to the oxygen vacancies concentration. According to these authors, the catalytic activity depends on the oxygen vacancies generated by the introduction of a metal into the CeO_2 structure, but it does not depend on the chemical nature of the dopant metal. Liu et al. [18] proposed that NO can adsorb as nitrites or nitrates on CeO_2 surface and then be dissociated by adjacent oxygen vacancies generated by surface reduction with CO.

In this context, we aim to study the effect of Fe incorporation into CeO_2 on the structure and morphology of these materials and consequently on the selective catalytic reduction reaction of NO_x using CO as reducing agent.

2 Experimental

2.1 Mixed Oxides Preparation

We prepared $Ce_{1-x}Fe_xO_{2-\delta}$ mixed oxides (x = 0; 0.05; 0.1; 0.15 and 0.2) following Pechini methodology by mixing 0.4 mol/L $Ce(NO_3)_3 \cdot 6H_2O$ (Aldrich chemistry, 99.0 %) and 0.1 mol/L $Fe(NO_3)_3 \cdot 9H_2O$ (Acros Organics, 99.0 %) solutions at room temperature in appropriate amounts for obtaining the desired Ce/Fe ratio. A 0.5 mol/L citric acid (CA) (Vetec, 99.5 %) solution was added into the Ce–Fe-containing solution under stirring, now at 60 °C and soaking for 30 min. The molar ratio CA: metallic cations was 1.1: 1 to ensure complete metal ions complexation. Then ethylene glycol (EG) (Tedia, 99.0 %) was added in the CA: EG molar ratio of 3: 2, while the temperature increased up to 90 °C. After approximately 3 h, a polymeric resin was obtained, dried at 110 °C for 12 h and calcined in a muffle at 300 °C for 30 min and at 500 °C for 5 h (1 °C/min).

2.2 Mixed Oxides Characterization

Thermogravimetric analysis (TGA) was performed to examine the thermal behavior of the dried resins synthesized by Pechini method on a SDT Q600 equipment. 10 mg of the samples were heated from room temperature to 700 °C at a heating rate of 20 °C/min in 100 mL/min of synthetic air flow. Calcium oxalate (CaC_2O_4) was employed as reference material.

The chemical composition of the mixed oxides was determined by X-ray fluorescence (XRF) on a Rigaku RIX 3100 equipment with rhodium tube as X-rays source. Textural properties were investigated by N_2 physisorption at −196 °C in ASAP equipment, Model 2000 (Micrometrics®). Pore size distribution was obtained by the BJH method from the desorption isotherm. Pretreatment of the samples consisted of drying at 300 °C under vacuum for 24 h.

XRD patterns were recorded on a Rigaku diffractometer, Model Miniflex, with copper radiation (CuKα λ = 1.5418 Å) within Bragg angle range of $10° \leq 2\theta \leq 90°$, with 0.05° step size and counting time of 2 s per step. The crystallite sizes were calculated by Scherrer equation. Rietveld method was employed to refine the XRD experimental data using the FullProf Suite® software.

The morphology of the samples was examined by FEG-SEM (Field Emission Gun Scanning Electron Microscope) on a FEI Company microscope, Model Quanta 400 operated at an accelerating voltage of 30 kV. Images were acquired using a secondary electrons detector. SEM analysis with X-ray energy dispersive detectors (EDS) was performed to examine the spatial distribution of the elements and to obtain semi-quantitative information of the surface chemical composition of the samples.

UV–Vis diffuse reflectance spectroscopy (UV–Vis DRS) was used to identify the coordination states of the species in the samples and to estimate the band gap of the catalysts. The analysis was performed on a Varian Cary 5000 device. Spectra were obtained in the wavelength range of 200–800 nm, and $BaSO_4$ was used as reference. Schuster–Kubelka–Munk (SKM) function, expressed by Eq. (2), was used to present the spectra.

$$F(R) = \frac{(1 - R)^2}{2 \cdot R} \tag{2}$$

in which R is the reflectance given by $R = 10^{-A}$ (A = absorbance).

F(R) curves were deconvoluted by Gaussian–Lorentzian fits by using PeakFit® software to obtain the contribution of the individual coordination states of the elements.

2.3 Catalytic Evaluation

We evaluated $Ce_{1-x}Fe_xO_{2-\delta}$ mixed oxides in the selective catalytic reduction (SCR) of NO by CO at room pressure

using a glass reactor coupled to a resistive oven with a PID temperature programmer. We measured the reaction temperature by a thermocouple placed at the outer wall of the reactor but alongside the catalyst bed. 75 mg of the catalyst (106–177 μm) were diluted with inert pretreated silica gel (Sigma-Aldrich, pore size 150 Å, 106–177 μm, calcined at 700 °C, 3 h, 5 °C/min in a muffle, static air) at the wt/wt proportion of catalyst:inert 1:5 (interparticle dilution).

Prior to the catalytic tests, we pretreated the samples by drying (300 °C, 1 h, 10 °C/min, 50 mL/min of He), reducing (350 °C, 1 h, 10 °C/min, 50 mL/min of H_2), then keeping at 350 °C for 1 h in He flow and finally cooling down to room temperature in He flow. Catalytic tests were carried out in a total flow 75 mL/min of a 0.5 % v/v NO, 0.5 % v/v CO and He balance flow (WHSV = 60,000 cm^3/(g_{cat}.h)). We investigated the temperature range of 100–350 °C.

Effluent gases from reactor were analyzed in parallel by a gas chromatograph (Agilent 7820A GC) equipped with a thermal conductivity detector (TCD) and by a gas analyzer TESTO Model 350 XL. The compounds NO, CO, N_2, N_2O and CO_2 were separated by a capillary column (Supelco Mol Sieve 5A Plot, 30 m × 0.32 mm) in the GC with He as carrier gas, whereas NO, NO_2, CO and O_2 were measured by electrochemical cells at TESTO instrument. We calculated NO and CO conversions by taking into account data from TESTO instrument, while selectivity to N_2 and N_2O from GC measurements. Commercial mixtures of 1 % NO/He and 5.1 % CO/He were purchased from Linde Industrial Gases.

NO and CO adsorption experiments were performed in a transient regime at room temperature by flowing the reaction mixture through the pre-reduced $Ce_{1-x}Fe_xO_{2-\delta}$ mixed oxides. NO, CO, NO_2 and O_2 concentrations were monitored as a function of time by the gas analyzer TESTO 350 XL.

3 Results and Discussion

3.1 Thermogravimetric Analysis (TGA)

The catalytic precursors obtained as polymeric resins during the synthesis procedure contain a large amount of organic material, which must be eliminated by calcination. TGA analysis of the polymeric resins indicated the temperature ranges for decomposition, allowing us to determine appropriate calcination temperatures chosen as 300 and 500 °C. The results are shown in Fig. 1 and Table 1.

According to the TGA profiles (Fig. 1) for x = 0, 0.1 and 0.2, we verified two mass loss regions, the first occurring around 180 °C, and the second taking place between 230 and 370 °C (less sharp than the first region).

For temperatures lower than 180 °C, the mass loss is ascribed to water, and above 180 °C to the decomposition of organic compounds of the polymeric resin. Table 1 shows that the mass loss for CeO_2 is ca. 85 % and decreases from 90 to 59 % by increasing Fe content (from x = 0.05 to 0.2). We noticed opposite trend in the second mass loss region, for which mass loss increases as iron content also increases. These findings suggest that iron presence leads to a more difficult elimination of organic residues in the polymeric resin, shifting the decomposition of a relevant mass percentage to the temperature range of 250–350 °C. For this reason, we chose 300 °C as the temperature for the first calcination step, aiming to eliminate most of organic residues.

The DTA and DTG profiles (derivative gravimetric curves not shown here) are similar for lower temperatures and could be assigned to the same exothermic phenomenon (i.e., burning of organic material), but they are quite different in the second region. DTA peaks remain practically in the same positions (around 180 and 300 °C) for all the samples and possibly represent some crystallization into the mixed oxide structures. DTG peaks follow the same trend of the first mass loss region, shifting to higher temperatures for x = 0.05 and then to lower temperatures with further increase of iron content. The second mass loss region might be ascribed to the elimination of nitrate and carbonate species. Therefore, we assume there are two thermogravimetric events taking place at temperatures between 230 and 370 °C, which are the crystallization of the material and the elimination of nitrates and carbonates.

DTA profiles indicate a strong thermal exothermic behavior for all samples, wherein the exothermicity of the thermal events increases with iron content. Therefore, the second step of calcination procedure was performed at 500 °C under slow heating rate (1 °C/min) to avoid sintering and to eliminate organic compounds completely.

Pure CeO_2 oxide synthesized by the Pechini method and calcined in a two-step procedure (300 and 500 °C) is a pale yellow solid due to the $O^{-2} \leftarrow Ce^{+4}$ charge transfers [19], but as the iron content increases into the structure, the solid becomes darker tending to brown. This will be explained later by UV–Vis results.

3.2 X-Ray Diffraction Analyzes (XRD)

Figure 2 shows the XRD patterns of the $Ce_{1-x}Fe_xO_{2-\delta}$ mixed oxides for which we identified only peaks related to the CeO_2 phase (face-centered cubic structure, Fm-3m space group) for all samples.

The absence of XRD reflections associated to Fe-containing phases (Fe_2O_3 for instance) could suggest the formation of single phase $Ce_{1-x}Fe_xO_{2-\delta}$ solid solutions, or the presence of small extension FeO_x-particles which might
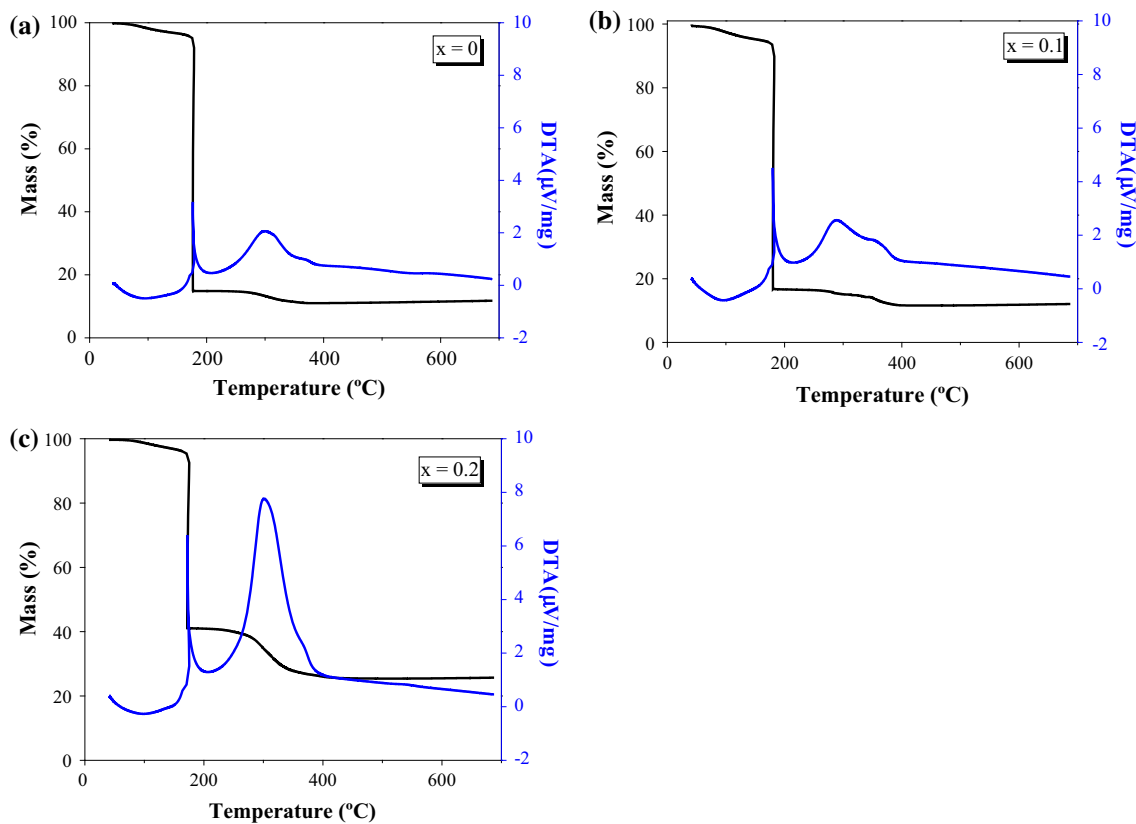
Fig. 1 Mass loss profiles obtained by thermogravimetry for the polymeric precursors of $Ce_{1-x}Fe_xO_{2-\delta}$ mixed oxides with x = 0; 0.1 and 0.2, respectively figures (**a**), (**b**) and (**c**). Profiles of DTA (differential thermal analysis) in *blue* represent the temperature difference between the catalyst sample and reference

Table 1 Data of mass loss and temperature during TGA analysis for polymeric precursors of $Ce_{1-x}Fe_xO_{2-\delta}$ mixed oxides synthesized by Pechini method

$Ce_{1-x}Fe_xO_{2-\delta}$	1st mass loss region (80–200 °C)			2nd mass loss region		
	Mass loss (%)	DTG peak (°C)	DTA peak (°C)	Mass loss (%)	DTG peak (°C)	DTA peak (°C)
x = 0	84.8	175	176	3.8	312	299
x = 0.05	90.4	181	182	2.5	375	300
x = 0.1	83.3	179	180	5.1	353	289
x = 0.15	64.5	170	167	11.9	345	296
x = 0.2	59.0	171	172	33.6	297	301

be undetectable in XRD measurements [9] (both hypotheses are not excluding). However, the Rietveld refinement which is a powerful method for quantifying crystalline phases in multiphase mixtures did not evidence any Fe-containing phase and actually showed that by increasing Fe^{+3} content, the lattice parameters (a,b,c) and interplanar distances of the (111) plane (here designated as $d_{(111)}$) decreased (see Table 2). These findings evidence a structural contraction of the unit cell and are consistent with the incorporation of Fe^{+3} into the CeO_2 lattice due to the smaller ionic radius of Fe^{+3} (0.64 Å) compared to Ce^{+4} (1.01 Å) [8, 9, 13, 20, 21], instead of Fe segregation.

Density is another property affected by changes in the sample composition as exhibited in Table 2. Density decreased 12 % after Fe^{+3} addition (x = 0.2) due to the partial substitution of Ce^{+4} cations (140.12 u) by Fe^{+3}, which is lighter (55.85 u) [22]. As shown in Fig. 3, the fitted diffractogram (polynomial function for the background and pseudo-Voigt Thompson Cox-Hastings for adjustment of the diffraction peaks) describes properly the
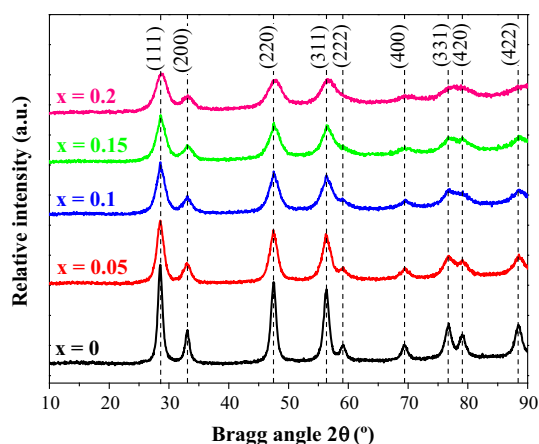
Fig. 2 XRD patterns of $Ce_{1-x}Fe_xO_{2-\delta}$ mixed oxides synthesized by the Pechini method and calcined in a two-step procedure (300 and 500 °C). *Dashed lines* indicate the diffraction positions for CeO_2 phase (JCPDS34-0394)

Fig. 3 XRD pattern of the $Ce_{0.8}Fe_{0.2}O_{2-\delta}$ mixed oxide refined by the Rietveld method

experimental data, enabling accurate calculation of the parameters shown in Table 2.

Bao et al. [9] synthesized Ce–Fe mixed oxides by co-precipitation using calcination temperature of 650 °C. The authors obtained single phase solid solutions for Fe molar percentages below 0.3; further increase in Fe content led to the formation of a second phase (i.e., segregated Fe_2O_3 crystallites). Laguna et al. [8] did not observe phase segregation for Ce–Fe mixed oxides with iron molar percentages up to 0.25 prepared by micro-emulsion and calcined at 500 °C.

Moog et al. [23] prepared $Ce_{1-x}Fe_xO_{2-\delta}$ mixed oxides by co-precipitation and microwave assisted process which led to x = 0.2 and x = 0.15, respectively, as the maximum iron content incorporated into CeO_2. According to Bao et al. [9], the limit of Fe^{+3} solubility in the CeO_2 structure depends on the synthesis conditions.

Figure 4 presents the linear variation of CeO_2 lattice parameter with increasing Fe^{+3} content according to Vegard's Law, which states that at a given temperature the cell parameter of a solid solution changes linearly with the concentration of its constituents [8].
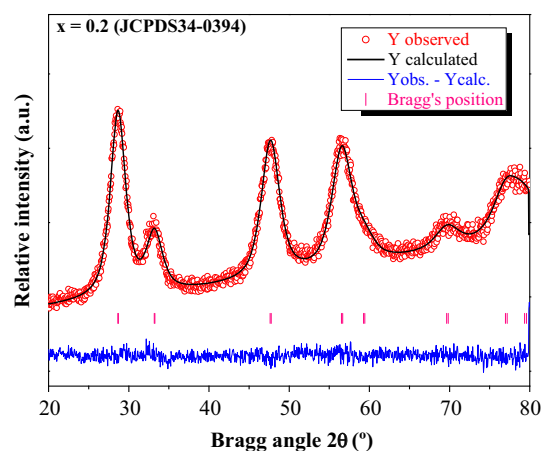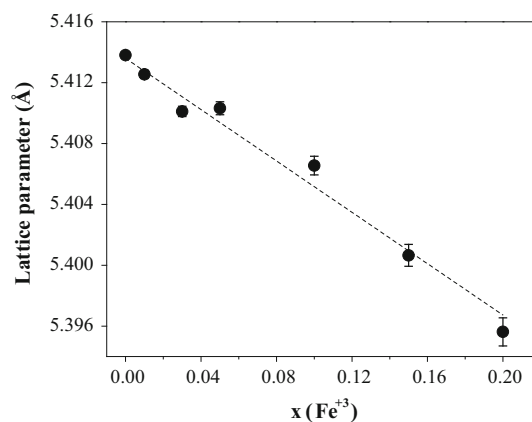

Fig. 4 Dependence of the CeO_2 lattice parameter (**a**) with Fe^{+3} doped content. *Dashed line* represents the linear fit of data given by the equation $y = 5.4136 - 0.084 \times x$ ($R^2 = 0.9659$)

Laguna et al. [8] reported a linear decrease in the lattice parameter of Ce–Fe mixed oxides with increasing iron content up to 10 %, but this trend did not remain for higher levels, suggesting greater difficulty for Fe insertion into the CeO_2 structure.

Table 2 Crystallographic information of the $Ce_{1-x}Fe_xO_{2-\delta}$ mixed oxides obtained through the refinement of XRD patterns by the Rietveld method

$Ce_{1-x}Fe_xO_{2-\delta}$	Unit cell parameters			2θ (°)	FWHM (°)	Crystallite size (nm)
	a = b = c (Å)	Density (g cm^{-3})	d(111) (Å)			
x = 0	5.413<u>81</u>(22)	7.147	3.1257	28.53	0.92	8.8
x = 0.05	5.410<u>32</u>(43)	6.953	3.1236	28.55	1.46	5.6
x = 0.1	5.406<u>55</u>(61)	6.752	3.1215	28.57	1.76	4.6
x = 0.15	5.400<u>65</u>(72)	6.536	3.1181	28.60	1.88	4.3
x = 0.2	5.395<u>62</u>(92)	6.277	3.1152	28.63	2.30	3.5

Wang et al. [24] obtained Ce–Fe mixed oxides by a CA sol–gel method with a two-steps calcination (at 300 and 500 °C), similar to the methodology we employed here. The authors did not observe phase segregation by XRD up to a doped iron content of 20 mol%. They observed a decrease in the lattice parameter by Rietveld refinement for doped iron content up to 5 mol%, however with increasing iron content to 7 mol% the lattice parameter increased. According to these authors, their results suggest gradual phase segregation with further increase of iron content, which means that Fe solubility in the CeO_2 is limited to 5 mol%. However, our results show that Ce–Fe solid solutions can have single phase for Fe content as high as 20 mol% when synthesized by Pechini method.

With increasing iron content into the Ce–Fe mixed oxides, the diffraction peaks become less intense and broader, as well as the (111) diffraction peak shifts towards higher 2θ values, as shown in Table 2. These findings suggest that Fe leads to a decrease of the crystallite sizes in the solid solutions. We confirmed this hypothesis by calculating the average crystallite size from the full width at half maximum (FWHM) and 2θ values of CeO_2 (111) using Scherrer's equation. These results (see Table 2) show that average crystallite size decreases from 8.8 to 3.5 nm with increasing iron content from x = 0 to 0.2. Besides, the diffraction peak shift indicates a contraction of the CeO_2 unit cell due to Ce^{+4} replacement by Fe^{+3} (already discussed previously based on the cell parameters) caused by change of the metal–oxygen position and length [8, 12, 20, 23, 25]. The decrease of crystallite size observed for Ce–Fe mixed oxides may be ascribed to the presence of Fe dopant which could inhibit the sintering process during calcination [8], or due to surface energetic factors associated to the micro strain in the structure caused by the lattice contraction [12].

3.3 Chemical Composition by XRF and Textural Analyzes

Table 3 summarizes the chemical composition and textural properties of the synthesized mixed oxides, and Fig. 5 displays the N_2 adsorption/desorption isotherms and pore size distributions.

The chemical composition by XRF indicated iron content as expected for all samples, evidencing complete incorporation of iron into the CeO_2 structure.
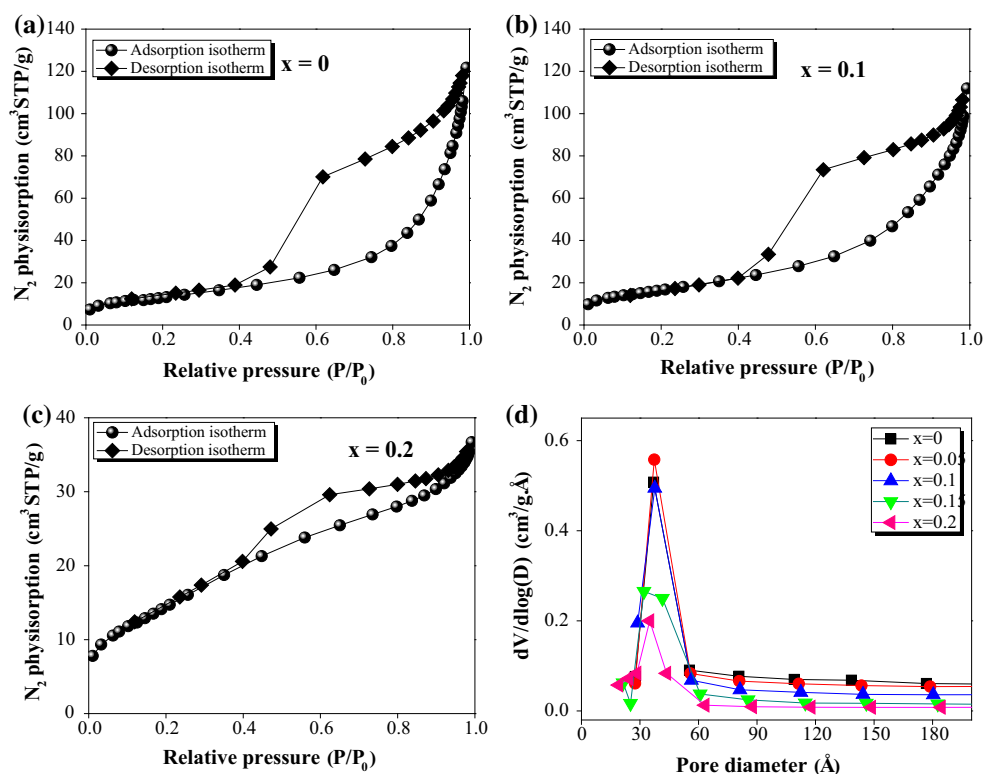
Though N_2 adsorption isotherms (Fig. 5a–c) resemble the Type II of IUPAC classification, which is typical of macroporous solids, these results do not agree with the pore size distribution which indicates mesoporous materials. Macroporosity is an unexpected feature for our mixed oxides since the crystallite sizes are relatively small (as shown in Table 2). Laguna et al. [8] reported the same behavior (Type II isotherms for Ce–Fe nanoparticles), however that would not correspond to macroporous, but to N_2 condensation in the inter-nanoparticles spaces. This statement might also explain our N_2 adsorption profiles. BJH pore size distribution (Fig. 5d) presented a narrow peak centered on 40 Å (unimodal pore size distribution) for all the mixed oxides, indicating the materials have mostly mesoporous [26]. The pore volume and average pore size decreased with increasing iron content.

BET specific surface area of undoped CeO_2 was 46 m^2/g. For $Ce_{1-x}Fe_xO_{2-\delta}$ mixed oxide with x = 0.05 the surface area did not change at all, but for x ≥ 0.1 the area increased slightly. In general trend in the literature [13, 20, 25] points to an enhancement of the surface area with Fe doping [26]. According to Jampaiah et al. [12], the increase in the specific surface area of doped CeO_2 is due to the inhibition of the particle growth caused by the ceria-dopant interaction. Shen et al. [13] reported an increase in the specific surface area of CeO_2 synthesized by the citrate method and calcined at 600 °C from 33 to 58 m^2/g when doped with 10 mol% of iron. Reddy et al. [27] observed surface area of Fe-doped CeO_2 prepared by co-precipitation and calcined at 550 °C behaving like the trend in Table 3, i.e., the specific surface area increased up to a Fe content of 10 mol%, and for higher Fe content the area remained higher than for CeO_2.

Table 3 Chemical composition and textural properties of the $Ce_{1-x}Fe_xO_{2-\delta}$ mixed oxides synthesized by Pechini method

$Ce_{1-x}Fe_xO_{2-\delta}$	Fe content (%)	Textural properties		
		Specific surface area (m^2/g)	Pore volume (cm^3/g)	Average pore diameter (Å)
x = 0	0	46	0.16	54
x = 0.05	5	47	0.16	52
x = 0.1	10	60	0.15	48
x = 0.15	15	53	0.09	44
x = 0.2	21	54	0.05	36

3.4 Scanning Electron Microscopy Analysis (SEM)

SEM images of CeO$_2$ and Ce$_{0.8}$Fe$_{0.2}$O$_{2-\delta}$ oxides are shown
in Fig. 6 with different magnifications (2 and 50 kX).

Figure 6 shows that Fe incorporation into the CeO$_2$
structure modifies its morphology. Undoped CeO$_2$ has a
spongy aspect, while the mixed oxide has a more com-
pacted and flat surface. It explains the decrease of pore
volume evidenced by the N$_2$ physisorption results. Figure 7
displays the distribution of Ce, Fe and O elements on the
surface of Ce$_{0.8}$Fe$_{0.2}$O$_{2-\delta}$ mixed oxide obtained by SEM–
EDS, and Table 4 presents semi-quantitative results for this
catalyst relative to cerium and iron concentration on the
particle surface.

Figure 7 indicates a uniform distribution of elements on
the surface of a Ce$_{0.8}$Fe$_{0.2}$O$_{2-\delta}$ particle. Complementing
this result, Table 4 shows that relative concentrations of Ce
and Fe elements on the surface of Ce$_{0.8}$Fe$_{0.2}$O$_{2-\delta}$ are
similar to the nominal composition. Therefore, Pechini
method is suitable for obtaining mixed oxides with desired
stoichiometry, as stated by Popa e Kakihana [21].

3.5 UV–Vis Diffuse Reflectance Spectroscopy Analysis (DRS)

UV–Vis DRS spectra of the Ce$_{1-x}$Fe$_x$O$_{2-\delta}$ mixed oxides
are displayed in Fig. 8. The DRS profiles show different
line shapes and bands. From these data we identified the

coordination state of the species, and estimated the band
gap. Thus, after deconvoluting F(R) curves, we obtained
the contribution of individual coordination states. Fig-
ure 8a, b show two calculated absorption bands for x = 0
and 0.05, respectively. Samples with higher Fe content
exhibited three calculated absorption bands. Table 5 shows
in detail the quantitative results for all samples.

Figure 8 shows that all samples absorb strongly the
radiation of the UV 200–400 nm. All the mixed oxides
exhibited two absorptions bands in the UV region, while
the oxides with x = 0.1, 0.15 and 0.2 also showed one
absorption band in the visible region (400–700 nm).

There is a controversy in the literature about the phys-
ical meaning of these absorption bands. Regarding the
bands in the UV region, some authors [12, 18, 22, 28],
attributed band 1 to the O 2p (O^{-2}) → Ce 4f (Ce^{+4}) charge
transfer, and band 2 to the inter-band transfer. On the other
hand, Hong et al. [11] associated the absorption band
around 285 nm to the Fe^{+3} (isolated ions) ← O charge
transfer, and the band around 350 nm to Fe$_x^{+3}$O$_y$ oligomer
clusters. Here in our DRS spectra for Ce–Fe mixed oxides
we observed these two bands even in the absence of iron
(i.e., for pure CeO$_2$), making sense to ascribe those UV-
region bands (200–400 nm) to O 2p (O^{-2}) → Ce 4f (Ce^{+4})
charge transfer and inter-band transfer.

We also noticed that as Fe content increased, bands 2
and 3 became broader and shifted towards higher wave-
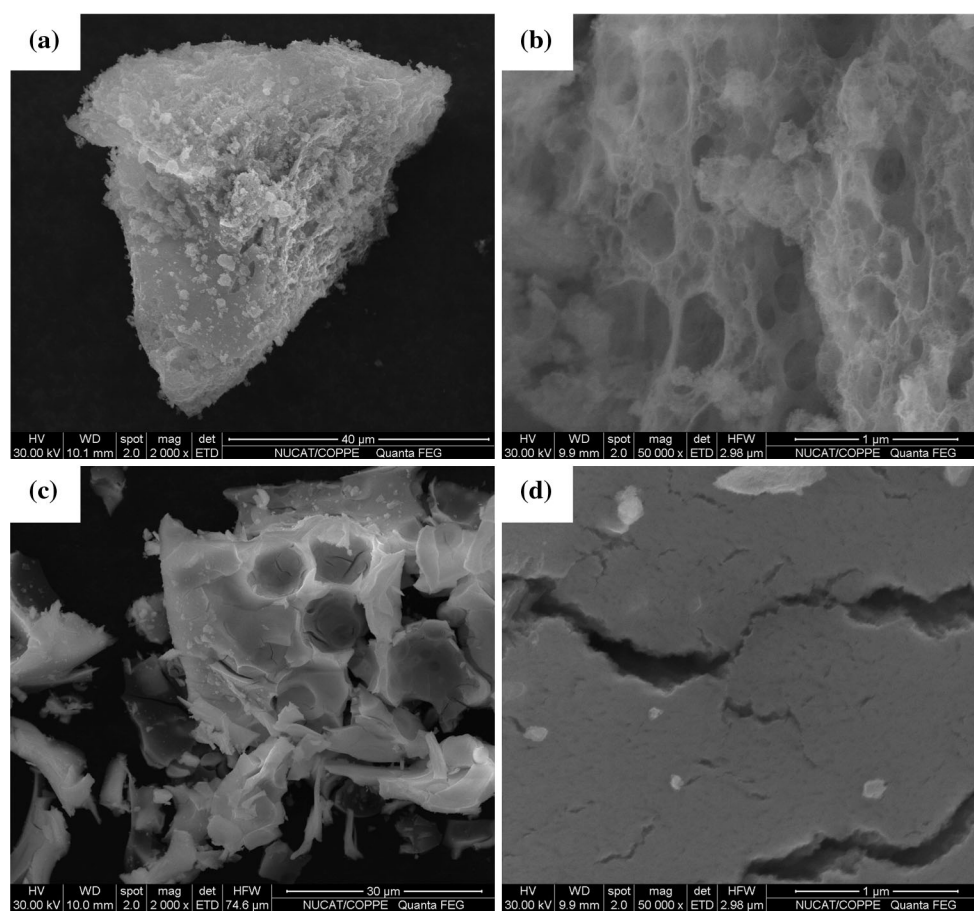lengths. According to Wang et al. [20] and Yue and Zhang

Fig. 6 SEM images of $Ce_{1-x}Fe_xO_{2-\delta}$ oxides synthesized by Pechini method; **a** CeO_2—2 kX, **b** CeO_2—50 kX **c** $Ce_{0.8}Fe_{0.2}O_{2-\delta}$—2 kX, **d** $Ce_{0.8}Fe_{0.2}O_{2-\delta}$—50 kX

[29], this phenomenon is due to the charge transfer transitions between Fe^{+3} 3d electrons and the conduction band (O 2p) and valence band (Ce 4f), since the dopant energy level is located within the CeO_2 band gap. For this reason, the sample color changes from yellow to brown as Fe content increases.

Yao et al. [28] attribute the shift of the absorption edges to the decrease of the symmetry of the CeO_2 structure due to the incorporation of Zr^{+4}, Sn^{+4} and Ti^{+4} species with formation of stressed solid solutions. According to these authors, the decrease of the grain size leads to the broadening of the absorption bands.

Laguna et al. [8] observed the main absorption band of α-Fe_2O_3 in the visible region around 533 nm. We did not observe this band here, which strongly evidences no segregation of iron as α-Fe_2O_3 and supports the hypothesis of single phase Ce–Fe solid solution for all samples.

Moreover, the electronic transition mode (direct or indirect) between the valence and the conduction bands for CeO_2-based materials is another matter of debate in the literature. Many authors [8, 20, 29] simply assume this electronic transition mode as the direct one, i.e., electronic

transition from the valence band to the conduction band taking place with photon emission. Band gap energy can be calculated by Eq. (3).

$$(h \cdot v \cdot \alpha)^{\frac{1}{n}} = A \cdot (h \cdot v - E_g) \qquad (3)$$

in which h·v is the incident photon energy, α is the absorption coefficient, A is a constant, E_g is the band gap energy and n depends on the electronic transition mode (for direct transition, n = 1/2).

The band gap of the $Ce_{1-x}Fe_xO_{2-\delta}$ mixed oxides were obtained by extrapolation of the linear portion of the $[F(R).hv]^2$ versus hv plots to F(R) = 0 (Fig. 9), in which F(R) is the Schuster–Kubelka–Munk function and is proportional to the absorption coefficient. Table 6 presents the calculated band gap values.

We found band gap energy for pure CeO_2 as 3.16 eV. Yue and Zhang [29] found a similar value of 3.07 eV. By increasing Fe content in our samples, the band gap energy decreased, indicating an improvement of the electronic structure, which means an easier electron transport. In fact, Fe^{+3} provides 3d unoccupied orbitals with lower energy than those from Ce 4f, reducing thereby the necessary
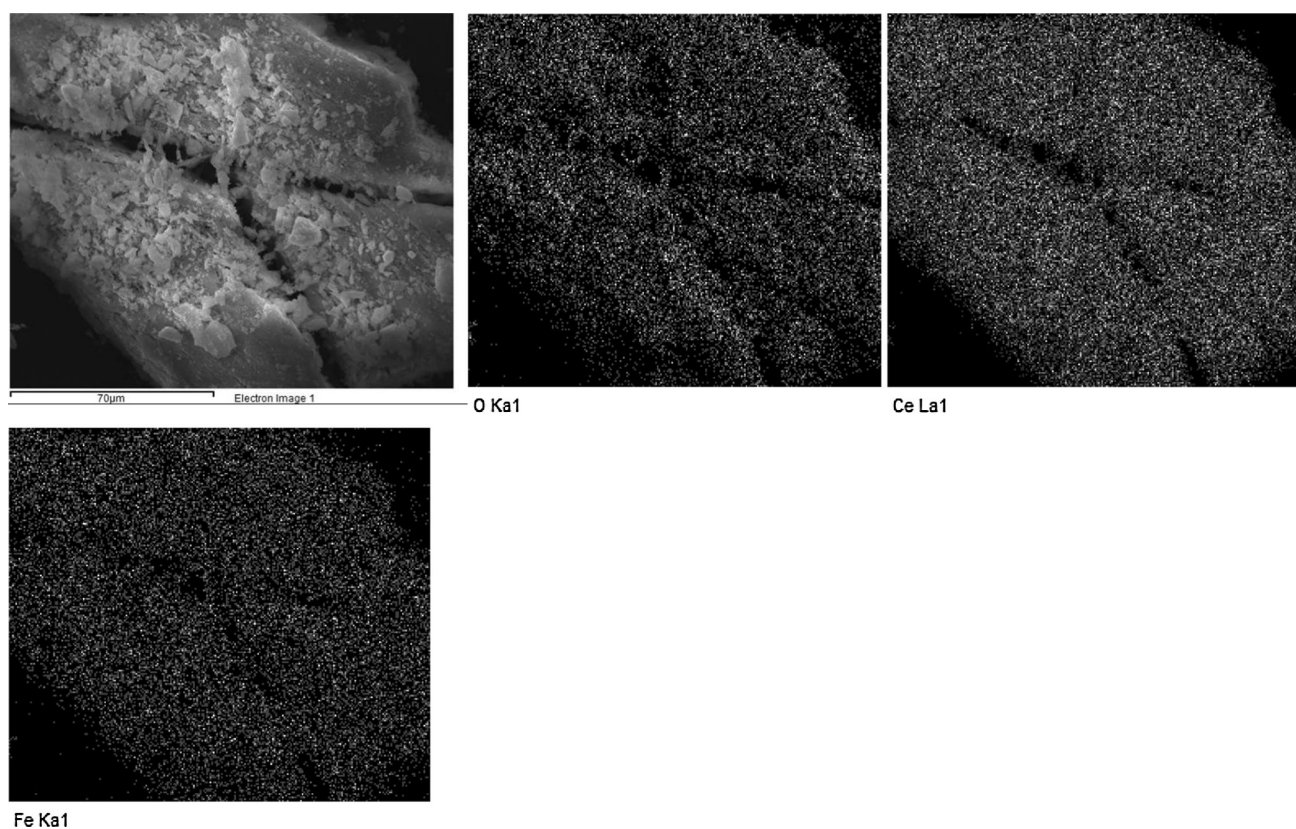
Fig. 7 SEM–EDS images of the $Ce_{0.8}Fe_{0.2}O_{2-\delta}$ mixed oxide synthesized by Pechini method

Table 4 Relative concentration of Ce and Fe elements on the surface of $Ce_{0.8}Fe_{0.2}O_{2-\delta}$ particle determined by scanning electron microscopy with X-ray energy dispersive detector

Element	Atomic percentage (%)	Nominal composition (%)
Ce	81.4	80
Fe	18.6	20

energy for electron transition from the O 2p orbital to the incomplete orbitals [8, 21]. Yue and Zhang [29] also reported decreasing band gap energy for CeO_2 doped with Ti, Mn, Fe and Co.

3.6 Catalytic Evaluation

3.6.1 Evaluation of $Ce_{1-x}Fe_xO_{2-\delta}$ Mixed Oxides in the NO-SCR by CO

The performance of the $Ce_{1-x}Fe_xO_{2-\delta}$ mixed oxides in the NO-SCR by CO reaction is displayed in terms of NO and CO conversions as a function of temperature in Figs. 10, 11, respectively.

Undoped CeO_2 showed the worst performance in the reaction, presenting NO and CO conversions below 15 % within all the range of temperature investigated. Iron

incorporation into the CeO_2 structure enhanced the catalytic activity. Both NO and CO conversions increased as a function of temperature and as a function of iron content.

NO and CO conversions were detectable above 150 °C and increased with temperature for all the Fe-doped samples. In the range of 150–250 °C, NO conversions were higher than CO conversions, but above 300 °C, they became similar. Figure 12 displays the selectivity to N_2 as a function of temperature for the $Ce_{1-x}Fe_xO_{2-\delta}$ mixed oxides.

Selectivity to N_2 increased with increasing temperature and iron content. From room temperature to 200 °C, the N_2 formation was not significant (less than 3 % for all samples), since the reaction proceeds towards N_2O formation. However, the selectivity to N_2 increased markedly above 250 °C, reaching 100 % at 350 °C, except for the undoped CeO_2. Yao et al. [28] also reported an enhancement in the NO conversion and selectivity to N_2 when CeO_2 was doped with Zr^{+4}, Ti^{+4} and Sn^{+4}. These authors proposed that CO can reduce Ce–M solid solutions (M = Zr, Ti and Sn) above 250 °C, creating oxygen vacancies and surface Ce^{+3} species. According to these authors, the oxygen vacancies would weaken N–O bond, enabling NO molecule to dissociate on the surface. Simultaneously, surface Ce^{+3} species would act as adsorption sites for CO_x, allowing CO_2
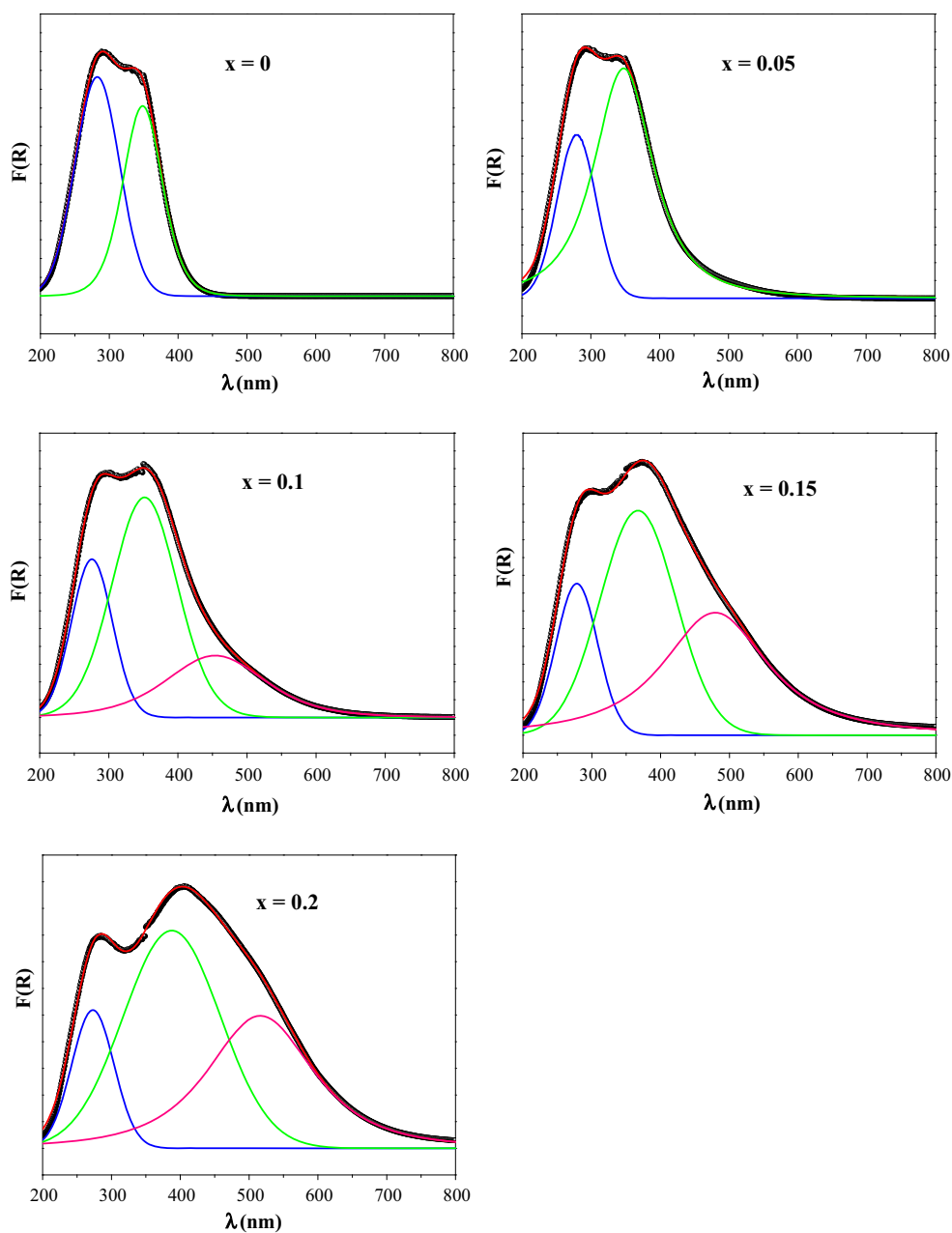
Fig. 8 UV–Vis DRS spectra of the Ce$_{1-x}$Fe$_x$O$_{2-\delta}$ mixed oxides. *Red line* is the calculated DRS spectra; *blue*, *green* and *pink lines* represent the deconvoluted curves obtained from the fitted spectrum

Ce$_{1-x}$Fe$_x$O$_{2-\delta}$	Band 1 (blue)		Band 2 (green)		Band 3 (pink)	
	λ (nm)	Percent area (%)	λ (nm)	Percent area (%)	λ (nm)	Percent area (%)
x = 0	282	55.0	349	45.0	–	–
x = 0.05	278	28.6	348	71.4	–	–
x = 0.1	275	23.3	352	52.7	454	24.0
x = 0.15	278	16.5	367	44.5	479	39.0
x = 0.2	273	13.6	386	49.5	516	36.9

Table 5 Quantitative data calculated from UV–Vis DRS spectra of the Ce$_{1-x}$Fe$_x$O$_{2-\delta}$ mixed oxides
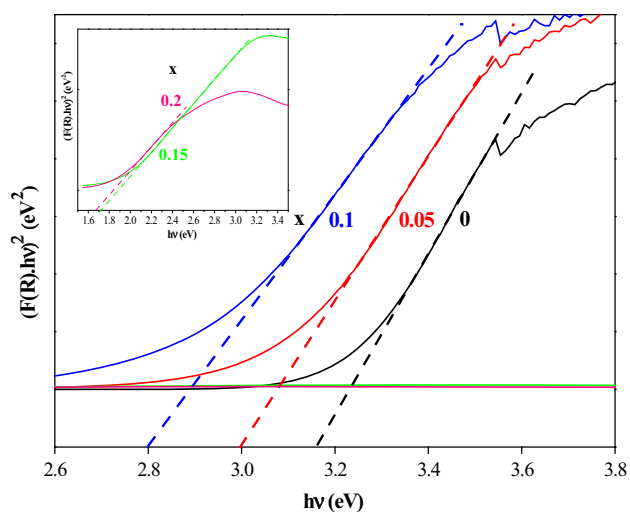
Fig. 9 Plot of $[F(R).h\nu]^2$ versus $h\nu$ with linear fits to obtain the direct band gap values for the $Ce_{1-x}Fe_xO_{2-\delta}$ mixed oxides

Table 6 Band gap of the $Ce_{1-x}Fe_xO_{2-\delta}$ mixed oxides obtained from UV–Vis DRS spectra

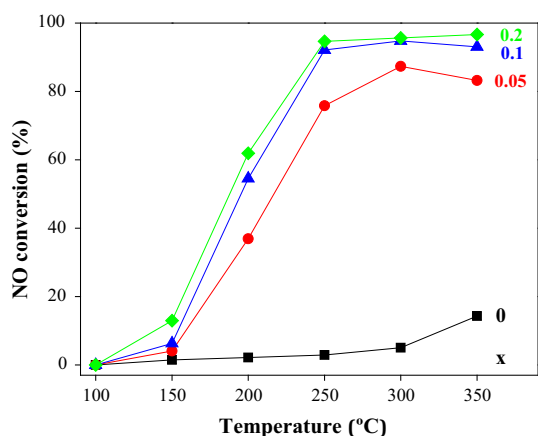| $Ce_{1-x}Fe_xO_{2-\delta}$	Band gap (eV)
x = 0	3.16
x = 0.05	3.00
x = 0.1	2.79
x = 0.15	1.73
x = 0.2	1.67

Fig. 10 NO conversion as a function of temperature for $Ce_{1-x}Fe_x$ $O_{2-\delta}$ mixed oxides with x = 0; 0.05; 0.1 and 0.2. Reaction conditions: 0.5 % v/v NO, 0.5 % v/v CO, He balance, WHSV = 60,000 cm³/(g$_{cat}$.h)

and N_2 formation. The authors also suggested that the decrease of grain size enhances Ce^{+3} species on the surface, consequently increasing the catalytic activity for NO abatement.
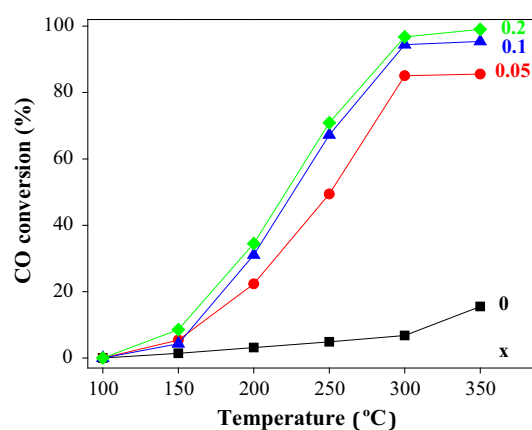

Fig. 11 CO conversion as a function of temperature for $Ce_{1-x}Fe_x$ $O_{2-\delta}$ mixed oxides with x = 0; 0.05; 0.1 and 0.2
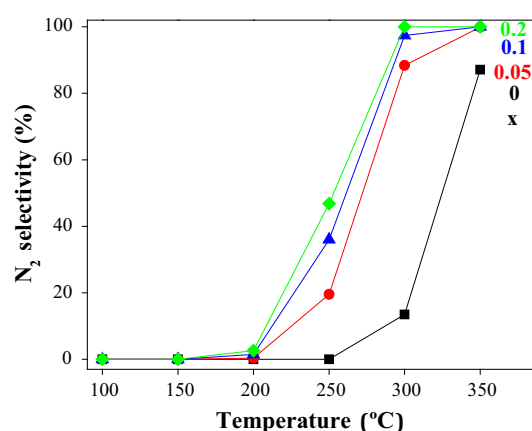

Fig. 12 Selectivity to N_2 as a function of temperature for $Ce_{1-x}Fe_x$ $O_{2-\delta}$ mixed oxides with x = 0; 0.05; 0.1 and 0.2

3.6.2 Interaction of NO and CO Molecules with $Ce_{1-x}Fe_xO_{2-\delta}$ Mixed Oxides at Room Temperature

To understand the interaction of NO and CO molecules with the surface of Ce–Fe oxides, we flowed the reaction mixture through the pretreated catalysts (reduction conditions detailed in Sect. 2.3) at room temperature. We monitored NO, CO, NO_2 and O_2 concentration as a function of time by using a gas analyzer TESTO 350 XL (this is a qualitative transient experiment). Figure 13 shows the profiles for distinct $Ce_{1-x}Fe_xO_{2-\delta}$ oxides and for the experiment in the absence of catalyst.

Figure 13a shows NO and CO concentration varying as a function of time as these compounds flow through the reactor in the absence of catalyst. Since the reactor had been previously sealed with helium, the disturbance in the CO and NO signals are due to the reactor dead volume (helium stuck in the reactor flows and drops NO and CO signals upon detection). On the other hand, Fig. 13b–d

Fig. 13 Concentration of gases (NO, CO, NO_2 and O_2) as a function of time during adsorption experiments of NO and CO on: **a** no catalyst; **b** $CeO_{2-\delta}$; **c** $Ce_{0.9}Fe_{0.1}O_{2-\delta}$; **d** $Ce_{0.8}Fe_{0.2}O_{2-\delta}$. *Dashed line* indicates the time in which the reaction mixture containing NO and CO was admitted into the reactor
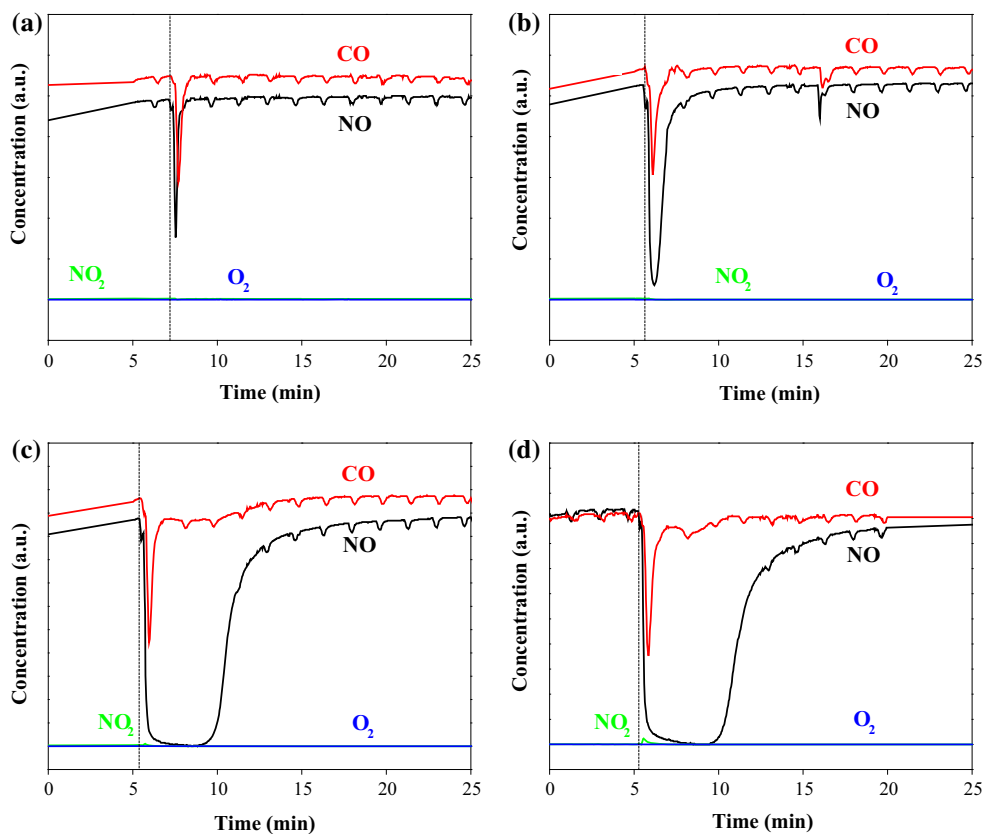
evidence that CO and mainly NO profiles behave differently in the presence of Ce–Fe mixed oxides, i.e., as soon as the reaction mixture was admitted into the reactor (see dashed line), NO was converted for a few minutes at room temperature. However, CO was practically unconverted (we should keep in mind we have to discount the reactor dead volume for NO and CO, showed in Fig. 13a, from all respective profiles). The higher the Fe content in the mixed oxide (up to x = 0.2), the longer the NO concentration remained very low, which means higher NO conversion into other compounds. Over time, the NO concentration was reestablished, reaching values similar to the original feed. That suggests the catalyst surface lost ability to convert NO.

After the experiments, we noticed that samples did not have a dark gray color typical of H_2-reduced materials anymore. Samples had the original color again (color before reduction), which strongly evidences that catalysts reoxidized during this NO–CO adsorption experiment.

Since the gas analyzer allowed us to identify only NO_2 during NO conversion (our TESTO equipment did not detect N_2, N_2O and CO_2), we performed GC analysis of the outlet gas after 2 min the reaction mixture was admitted into the reactor. For all the catalysts, we detected N_2 and N_2O by chromatography at this time, but no CO_2, which suggests absence of CO oxidation at room temperature.

Therefore, $Ce_{1-x}Fe_xO_{2-\delta}$ mixed oxides have the ability to dissociate NO molecules even at room temperature, leading to N_2 and N_2O, but cannot oxidize CO at this condition. We did not identify O_2 formation during the adsorption experiment, but some NO_2 has been detected in negligible amount on $Ce_{1-x}Fe_xO_{2-\delta}$ with x = 0.1 and 0.2. In this sense, oxygen atoms coming from NO dissociation lead to N_2O formation (by reacting with N_{ads} adsorbed species) and/or reoxidize the catalyst surface.

To obtain more insights on the surface, we investigated NO adsorption on CeO_2 and $Ce_{0.9}Fe_{0.1}O_{2-\delta}$ oxides (previously reduced in H_2) by monitoring NO consumption and products formation using mass spectroscopy. Figure 14 shows the results. According to Fig. 14a, we verified that on CeO_2, NO was partially converted to N_2, but mostly to N_2O. On the other hand, on $Ce_{0.9}Fe_{0.1}O_{2-\delta}$ mixed oxide (Fig. 14b), NO was initially and mostly converted to N_2. After N_2 reached a maximum concentration, it continuously decreased. Simultaneously, N_2O concentration increased and remained until NO was not converted neither to N_2 nor N_2O over time. We attribute the distinct performances of CeO_2 and $Ce_{0.9}Fe_{0.1}O_{2-\delta}$ during NO adsorption experiments to the oxygen vacancies concentration on the surface, which is probably higher for the Ce–Fe mixed oxide.

Based on these findings, we proposed a route for NO adsorption on $Ce_{1-x}Fe_xO_{2-\delta}$ mixed oxides similar to the

Fig. 14 Concentration of NO, N_2 and N_2O as a function of time during NO adsorption experiment on **a** CeO_2 and **b** $Ce_{0.9}Fe_{0.1}O_{2-\delta}$ oxides. *Dashed line* indicates the time in which the reaction mixture containing NO was admitted into the reactor
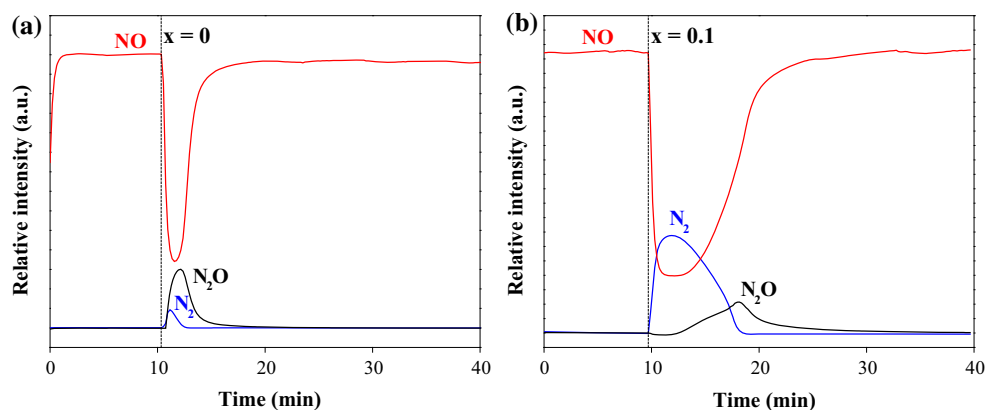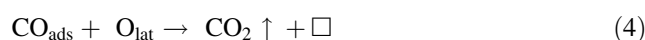

scheme proposed by Daturi et al. [30] for NO adsorption on CeO_2 and on $Ce_{1-x}Zr_xO_{2-\delta}$ mixed oxides. Initially, the reduction procedure generates a high concentration of oxygen vacancies on the catalyst surface. As soon as NO flow is admitted onto the catalyst bed, NO molecules adsorb on the surface oxygen vacancies. Due to the abundance of anionic vacancies, NO molecules may adsorb on adjacent sites, favoring a chemical bond between N terminal atoms of NO adsorbed species, leading to N_2 formation, while the O terminal atoms of NO adsorbed species partially reoxidize the surface.

As a consequence of the surface partial reoxidation, the oxygen vacancies become farther away from each other, hindering the N–N chemical bond formation and consequent N_2 release. At this point, the reaction between the N terminal atom of adsorbed NO species and NO molecules in the gas phase would rather take place (Eley–Rideal mechanism), leading to N_2O instead of N_2. When the surface becomes completely reoxidized (and no oxygen vacancies are available), NO chemisorption does not take place anymore.

Daturi et al. [30] investigated the NO adsorption on ceria and ceria-zirconia mixed oxides. The authors observed the formation of N_2, but not N_2O during the adsorption process. They attributed the NO conversion to the oxygen vacancies of the samples. According to them, the NO molecules can adsorb and dissociate at the same time on the oxygen vacancies. Silveira et al. [31] also reported N_2 and N_2O release during NO adsorption at room temperature on previously reduced $Ce_{1-x}Zr_xO_{2-\delta}$ mixed oxides.

Based on our NO and CO adsorption transient experiments at room temperature, we try to explain the catalytic performance shown in Figs. 10, 11, 12 for different temperatures (from room temperature up to 350 °C) in terms of surface oxygen vacancies, which are important for NO dissociation. At relatively low temperatures (up to 100 °C), the NO reduction by CO does not take place because the surface of Ce–Fe mixed oxides remains oxidized. At 150

and 200 °C, the NO and CO are converted to CO_2 and N_2O, according to the following reactions:

$$CO_{ads} + O_{lat} \rightarrow CO_2 \uparrow + \square \quad (4)$$

$$NO_{ads} + \square \rightarrow N_{ads} + O_{lat} \quad (5)$$

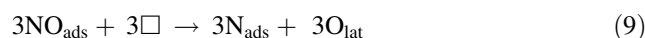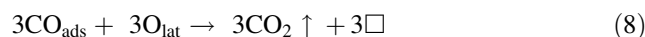$$NO_{ads} + N_{ads} \rightarrow N_2O \uparrow \quad (6)$$

in which the subscript *ads* indicates adsorbed species, O_{lat} and $\square$ represent lattice oxygen and oxygen vacancy, respectively.

Equations (4–6) lead to the global reaction:

$$2NO + CO \rightarrow N_2O + CO_2 \quad (7)$$

The reaction stoichiometry explains the higher NO consumption relative to CO. At the range of 150–200 °C, CO probably reduces the surface by removing O_{lat} and forming CO_2 and an oxygen vacancy. However these oxygen vacancies are still far away from each other to allow N_2 formation. But adsorbed NO on the oxygen vacancies might react with gas phase NO, giving N_2O.

At 250 °C, reactions (Eq. 1 and 7) compete, forming N_2 and N_2O by the following steps:

$$3CO_{ads} + 3O_{lat} \rightarrow 3CO_2 \uparrow + 3\square \quad (8)$$

$$3NO_{ads} + 3\square \rightarrow 3N_{ads} + 3O_{lat} \quad (9)$$

$$N_{ads} + N_{ads} \rightarrow N_2 \uparrow \quad (10)$$

$$NO_{ads} + N_{ads} \rightarrow N_2O \uparrow \quad (11)$$

At higher temperatures (300 and 350 °C), the surface is more easily reduced by CO, giving CO_2 which desorbs leaving a high concentration of oxygen vacancies on the mixed oxides surface. As previously stated, the high concentration of surface oxygen vacancies favors N_2 formation.

Figure 15 summarizes the proposed general reaction route. N_2/N_2O ratio will be a function of the oxygen vacancies concentration. While adjacent vacancies tend to form N_2, the more isolated vacancies lead to N_2O. The concentration of oxygen vacancies on the surface will be a

Fig. 15 Proposed catalytic cycle for NO-SCR on $Ce_{1-x}Fe_xO_{2-\delta}$ involving removal of lattice oxygen by CO, and formation of N_2 or N_2O by adsorption of NO at vacancies
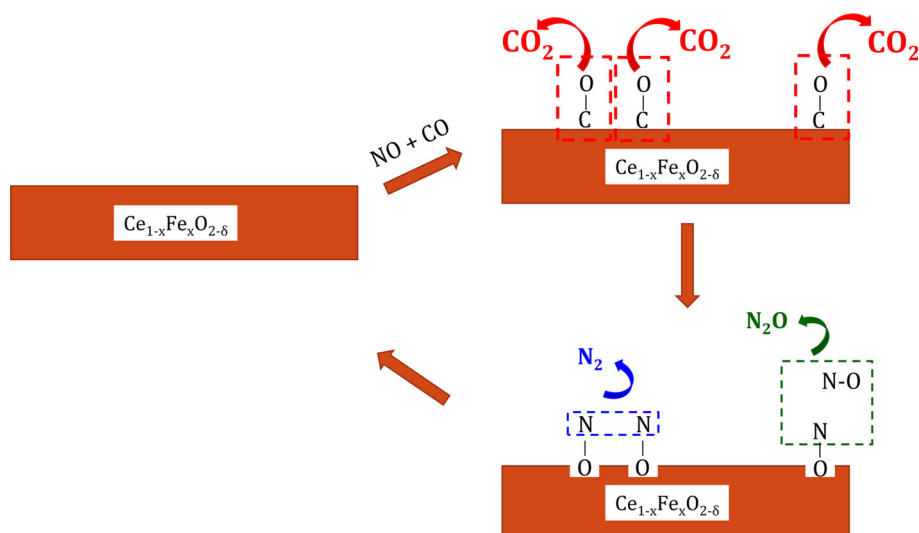
function of (i) iron content into the solid solution and (ii) reaction temperature.

The enhanced catalytic activity and N_2-selectivity with increasing Fe content in the CeO_2 structure is probably due to the greater and easier oxygen vacancies formation. Indeed, according to Trovarelli [6], the maintenance of the CeO_2 electro-neutrality when doped with aliovalent cations (M^{+2}/M^{+3}) can be achieved by one of three possible mechanisms known as: (i) compensation by vacancies (release of 1 mol of O^{-2} from the crystalline lattice for each 2 mol of Ce^{+4} that are replaced by M^{+3}), (ii) compensation by interstitial dopant (location of 1 mol of M^{+3} dopant in the interstitial sites of CeO_2 for each 3 mol of Ce^{+4} that are replaced by M^{+3}), and (iii) compensation by interstitial cerium (location of Ce^{+3} or Ce^{+4} species in the interstitial sites after dopant insertion).

According to the structural information obtained in this work by XRD and Rietveld refinement (i.e., a decrease in the lattice parameter indicating contraction of the unit cell), we confirm that iron was incorporated into the CeO_2 structure as Fe^{+3} in the position of Ce^{+4}. Thus, the electro-neutrality of the mixed oxides was kept through the mechanism of compensation by vacancies.

4 Conclusions

In this work, we prepared $Ce_{1-x}Fe_xO_{2-\delta}$ (x = 0; 0.05; 0.1 and 0.2) mixed oxides with desired stoichiometry by the Pechini method. All samples were single phase solid solution. The Fe incorporation into the CeO_2 structure led to a decrease in the (i) crystallite size, (ii) density, (iii) band gap, (iv) lattice parameter (contraction of the unit cell) and (v) porosity (probably due to the approximation of grains, decreasing interparticle spaces).

$Ce_{1-x}Fe_xO_{2-\delta}$ mixed oxides were evaluated in the NO reduction by CO. Undoped CeO_2 showed a poor performance in the reaction, but the mixed oxides were very active and selective to N_2, mainly within the range of 300–350 °C. The performance of the mixed oxides in the NO-SCR by CO reaction was enhanced by iron incorporation. We explained this finding by the action of surface oxygen vacancies arisen to maintain the electroneutrality of the solid structures.

According to our proposal, the surface concentration of oxygen vacancies increases as iron content in the Ce–Fe oxides increases. These vacancies have the ability to dissociate NO molecule, leading to N_2 formation mainly at high temperatures (250–350 °C). For lower temperatures (150–200 °C), N_2O formation rather takes place because CO is not able to reduce the surface to a great extent (creating vacancies) even for samples with higher Fe content.

Previously reduced $Ce_{1-x}Fe_xO_{2-\delta}$ mixed oxides were also able to dissociate NO molecules at room temperature to firstly form N_2 and then N_2O over time. This finding agrees with the proposed reaction route, because after the reducing pretreatment the concentration of oxygen vacancies is high, which allows N_2 formation, but over time the surface becomes mostly reoxidized leading preferentially to N_2O via an Eley–Rideal mechanism.

References

1. Roy S, Hegde MS, Madras G (2009) Appl Energ 86:2283–2297
2. Manahan SE (2004) Environmental chemistry, 8th edn. CRC Press, Boca Raton

3. Seinfeld JH, Pandis SN (1997) Atmospheric chemistry and physics: from air pollution to climate change. Wiley, New York
4. Cónsul JMD, Thiele D, Veses RC, Baibich IM (2004) Quim Nova 27:432–440
5. Aneggi E, Boaro M, de Leitenburg C, Dolcetti G, Trovarelli A (2006) J Alloy Compd 408–412:1096–1102
6. Trovarelli A (2002) Catalysis by ceria and related materials, vol 2, 1st edn. Imperial College Press, London
7. Wang J, Zhang B, Shen M, Wang J, Wang W, Ma J, Liu S, Jia L (2011) J Sol–Gel Sci Technol 58:259–268
8. Laguna OH, Centeno MA, Boutonnet M, Odriozola JA (2011) Appl Catal B Environ 106:621–629
9. Bao H, Chen X, Fang J, Jiang Z, Huang W (2008) Catal Lett 125:160–167
10. Qiao D, Lu G, Liu X, Guo Y, Wanh Y, Guo Y (2011) J Mater Sci 46:3500–3506
11. Hong W-J, Ueda M, Iwamoto S, Hosokawa S, Wada K, Kanai H, Deguchi H, Inoue M (2011) Appl Catal B Environ 106:142–148
12. Jampaiah D, Tur KM, Ippolito SJ, Sabri YM, Tardio J, Bhargava SK, Reddy BM (2013) RSC Adv 3:12963–12974
13. Shen Q, Lu G, Du C, Guo Y, Wang Y, Guo Y, Gong X (2013) Chem Eng J 218:164–172
14. Zhang Z, Han D, Wei S, Zhang Y (2010) J Catal 276:16–23
15. Pérez-Alonso FJ, Granados ML, Ojeda M, Terreros P, Rojas S, Herranz T, Fierro JLG (2005) Chem Mater 17:2329–2339
16. Pérez-Alonso FJ, Granados ML, Ojeda M, Herranz T, Rojas S, Terreros P, Fierro JLG, Gracia M, Gancedo JR (2006) J Phys Chem B 110:23870–23880
17. Pérez-Alonso FJ, Melián-Cabrera I, Granados ML, Kapteijn F, Fierro JLG (2006) J Catal 239:340–346
18. Liu L, Cao Y, Sun W, Yao Z, Liu B, Gao F, Dong L (2011) Catal Today 175:48–54
19. Rao GR, Mishra BG (2003) Bull Catal Soc India 2:122–134
20. Wang Y, Wang F, Chen Y, Zhang D, Li B, Kang S, Li X, Cui L (2014) Appl Catal B Environ 147:602–609
21. Popa M, Kakihana M (2002) Solid State Ion 151:251–257
22. Brito PCA, Santos DAA, Duque JGS, Macêdo MA (2010) Phys B 405:1821–1825
23. Moog I, Feral-Martin C, Duttine M, Wattiaux A, Prestipino C, Figueroa S, Majimel J, Demourgues A (2014) J Mater Chem A 2:20402–20414
24. Wang J, Shen M, Wang J, Cui M, Gao J, Ma J, Liu S (2012) J Environ Sci 24:757–764
25. Sudarsanam P, Mallesham B, Durgasri DN, Reddy BM (2014) RSC Adv 4:11322–11330
26. Leofanti G, Padovan M, Tozzola G, Venturelli B (1998) Catal Today 41:207–219
27. Reddy AS, Chen C-Y, Chen C-C, Chien S-H, Lin C-J, Lin K-H, Chen C-L, Chang S-C (2010) J Mol Catal 318:60–67
28. Yao X, Tang C, Ji Z, Dai Y, Cao Y, Gao F, Dong L, Chen Y (2013) Catal Sci Technol 3:688–698
29. Yue L, Zhang X-M (2009) J Alloy Compd 475:702–705
30. Daturi M, Bion N, Saussey J, Lavalley J-C, Hedouin C, Seguelong T, Blanchard G (2001) Phys Chem Chem Phys 3:252–255
31. Silveira EB, Perez CAC, Baldanza MAS, Schmal M (2008) Catal Today 133–135:555–559